Interface-Stabilized Phases of Metal-on-Oxide Nanodots

Riccardo Ferrando,[†,*] Giulia Rossi,[†] Florin Nita,[†,‡] Giovanni Barcaro,[§] and Alessandro Fortunelli[§,*]

[†]Dipartimento di Fisica and INFM/CNR, Via Dodecaneso 33, Genova, I16146, Italy, [‡]Institute of Physical Chemistry IG Murgulescu, Romanian Academy, Spl. Independentei 202, Bucharest, Romania, and [§]IPCF/CNR, Via G. Moruzzi 1, Pisa, I56124, Italy

ABSTRACT The control of the structure of oxide-supported metal nanoparticles is crucial in determining their properties and possible applications. Here, building principles are derived for predicting the epitaxies of metal nanoparticles on square-symmetry oxide surfaces. Unusual phases are found for an appropriate choice of the metal−oxide pair, where nanoparticles with hcp structure are stabilized for fcc metals such as Ni, Pd, and Pt, or for Co in a size range in which Co has typically nonhcp arrangements. These predictions are supported by a comparison with available experimental data on Ni/MgO(100) nanodots, and generalized to a whole class of metal−oxide systems of great potential interest, such as Pd and Pt on CaO, Ni on CoO, and Co on MgO. The atomistic features of the nanoparticles in turn suggest that these materials should possess peculiar properties; in particular, the facets exposed by the nanodots reveal adsorption sites with unusual geometry of possible effect on their catalytic properties, while the destabilization of stacking faults and the structural deformations observed for these particles are expected to influence their magnetic behavior.

KEYWORDS: nanoparticles · metals · oxides · surfaces · global optimization · density functional

As device miniaturization proceeds, attention is increasingly focusing on metal nanoparticles from a few tens to a few thousands of atoms, with applications ranging from catalysis to electronics, data storage, optics, and biological labeling.[1] The scientific and technological interest for these systems is further fueled by the discovery that at such small sizes unexpected structures may arise,[2−4] exhibiting novel and peculiar properties. In this context, oxide-supported metal nanoparticles have attracted great interest since a long time,[5] as they can be produced as dispersed objects with well-defined three-dimensional structures,[6] whose fine details are important in determining specific properties,[7−12] and whose control is crucial for developing new application devices. Their structure is ruled by a complex interplay of metal−metal and metal−oxide interactions,[13] but the possible scenarios and the corresponding building principles are far from being clarified.

Among oxide-supported metal systems, Pd/MgO(001) is one of the most extensively studied due to its importance as a model heterogeneous catalyst.[5] The MgO(001) surface is of square symmetry, with a checkerboard arrangement of alternating Mg and O atoms (lattice parameter 4.2072 Å, O−O distance 2.974 Å [14]). Metal atoms preferentially adsorb on top of oxygen atoms.[15] Bulk palladium is face-centered-cubic (fcc). Even though the nearest-neighbor distance in bulk Pd is smaller by about 7.5% than the distance between nearby adsorption sites on MgO(001), Pd nanoparticles easily grow in cube-on-cube fcc(001) epitaxy on the substrate.[5] Their morphology has been accurately determined,[13] and it has been shown that these nanoparticles present features, such as overhangs at the interface with the support, that can be strongly active sites for specific reactions.[11]

Metal−oxide systems presenting a larger size mismatch than Pd/MgO(001) have been much less investigated, despite their great potential interest. It can be expected, in fact, that a larger mismatch may cause the growth of "exotic" epitaxies, in which the nanodots have unusual morphologies. In the present work, we will focus on systems in which the mismatch between the bulk metal nearest-neighbor distance and the O−O distance in the substrate is in the range 15−20%, specifically considering Ni/MgO, Co/MgO, Pd/CaO, Pt/CaO, Au/CaO, and Ni/CoO(001), and we will show that, in an appropriate range of lattice mismatch, adhesion, and metallic energies, a general class of exotic hcp nanoparticle phases can be stabilized in a controlled way, even for metals that are not hcp in the bulk. In the following, Ni/MgO(001) is assumed as a

*Address correspondence to ferrando@fisica.unige.it, fortunelli@ipcf.cnr.it.

Received for review May 22, 2008 and accepted July 23, 2008.

Published online August 12, 2008.
10.1021/nn800315x CCC: $40.75

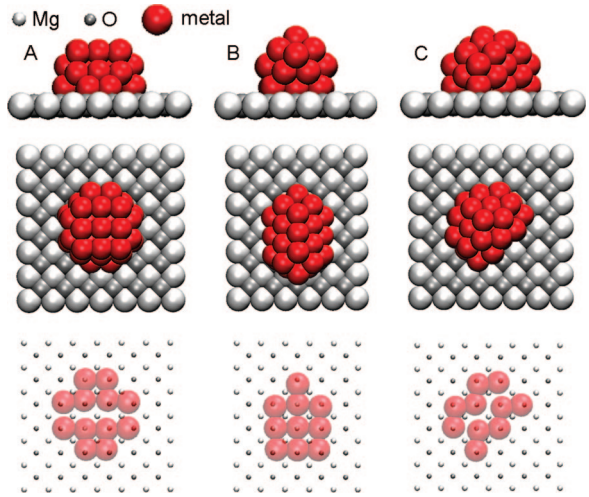

Figure 1. Representative structures of the three significant structural motifs of 40-atom Ni nanodots on MgO: (A) fcc(001) motif, (B) 5-fold motif, and (C) hcp motif. From top to bottom, side, top, and bottom views of the dots. The bottom view shows only the atoms that are in contact with the substrate. The energies of the nanoparticles are reported in Table 1.

testbed of our theoretical and computational approach. Electron-diffraction measurements have revealed the growth of small and medium-size Ni nanodots[16] that present vertical planes in hexagonal close-packed (hcp) stacking. The actual morphology of these nanodots and the nature of their exposed facets are, however, still unknown. At larger size, a transition toward the fcc(001) epitaxy occurs.[16,17] Our methodology will allow us to precisely determine the size-dependent morphology of the Ni/MgO(001) nanodots, and the size range in which hcp structures are energetically favorable, reproducing the size-dependent transition from hcp to fcc structures in remarkable agreement with the available experimental data.[16]

Pd and Pt are both bulk fcc metals of major interest in catalysis. CaO is an alkaline earth oxide as MgO, with which it shares the same bulk (rock salt) structure. However, apart from a larger lattice parameter (4.8032 Å [14]), CaO presents other interesting features as a support for the growth of metal particles, such as a stronger (by roughly ≈20%) metal−surface interaction and a more rugged energy landscape for metal adsorption. CoO in the rock salt form (lattice parameter 4.267 Å (ref 14)) can be stabilized in the form of thin or ultrathin films grown as buffer layers on the (100) surfaces of isomorphic oxides such as MgO or NiO.[18] An atomically sharp interface between a ferromagnetic metal and an antiferromagnetic oxide, as in Ni nanodots on CoO(100), is particularly interesting also as a model system in which to study the origin of the exchange bias effect.[19] Finally, the case of Co/MgO(001) is somewhat different. Even though bulk Co is hcp, the hcp phase is uncommon for nanoparticles of sizes below 4 nm (or even larger),[20,21] because Co nanoparticles prefer either icosahedral or fcc arrangements. If the substrate is properly chosen, its templating effect may stabilize the hcp phase also for small Co nanodots.

TABLE 1. DFT Results on the Energetics of Ni/MgO(001) Nanodots[a]

size	structure	E_{bind}	ΔE	E_{adh}	E_{met}
Ni_{30}	5-fold	−114.60	0.00	−7.46	−107.14
	hcp	−114.11	0.49	−7.15	−106.96
	fcc(001)	−113.91	0.69	−7.59	−106.32
Ni_{40}	hcp	−155.78	0.00	−8.71	−147.07
	5-fold	−155.42	0.35	−7.90	−147.52
	fcc(001)	−154.40	1.38	−8.68	−145.72
Ni_{50}	hcp	−197.70	0.00	−10.61	−187.09
	5-fold	−197.13	0.57	−9.51	−187.62
	fcc(001)	−196.64	1.06	−10.25	−186.39

[a] E_{bind} is the binding energy of the nanoparticle, ΔE is the energy difference from the lowest isomer, E_{adh} is the adhesion energy between the nanoparticle and the substrate, and E_{met} is the metallic atomization energy. All energies are in eV.

Our predictive computational methodology is based on an extensive search for structural motifs by means of global optimization methods[22] within many-body semiempirical potential models including metal−metal and metal−substrate interactions.[23] Sizes up to $N = 500$ atoms are considered. In the size range $N \leq 50$ atoms, the lowest-energy structures of each structural motif are then locally reoptimized by density-functional theory (DFT) calculations.[22]

RESULTS AND DISCUSSION

In the case of Ni/MgO(001), the global optimization searches in the size range $N \leq 50$ atoms single out three main structural motifs (see Figure 1). The first motif recalls the structure of bulk Ni. In fact, nanoparticles belonging to this motif are fcc nanocrystals which grow in (001) epitaxy with the oxide substrate. For this reason, this motif will be referred to as fcc(001) motif. However, due to the huge size mismatch between the nearest-neighbor distance in Ni and the O−O distance in the MgO substrate, these nanoparticles are often strongly distorted and/or dislocations between close-packed planes are observed. These dislocations, which appear already for very small sizes, help the structure in decreasing its strong internal strain. The second motif (referred to as 5-fold motif in the following) is noncrystalline. Nanoparticles belonging to this motif present at least one local 5-fold symmetry. Finally, the third motif is made of hcp nanocrystals, whose close-packed planes, alternating in ···ABAB··· stacking, are perpendicular to the oxide substrate and oriented along the [100] (or equivalently the [010]) direction of the substrate, thus in agreement with the electron-diffraction results.[16]

While for extremely small aggregates there is no clearly prevailing motif, as the size increases above ∼40 atoms, the hcp motif becomes more and more favorable, so that the lowest-energy structures are hcp for almost all sizes. The prevalence of the hcp motif is clear

from the results of DFT calculations reported in Table 1. For Ni_{30}/MgO(001), a 5-fold structure is more stable than the best hcp structure, which is however lower in energy than fcc(001) structures. For Ni_{40} and Ni_{50}/MgO(001), hcp structures are the most favorable, with increasing energy differences.

In order to discuss which factors favor the stability of hcp nanodots for these small sizes, we decompose the binding energy E_{bind} of the nanoparticles into the metallic atomization energy E_{met} and the adhesion energy E_{adh} between the nanoparticle and the substrate. The metallic energy E_{met} is calculated by separating the nanoparticle from the surface and calculating its energy without any further relaxation. The adhesion energy E_{adh} is the difference between E_{bind} and E_{met}. 5-fold structures have favorable metallic energy, but a bad matching with the substrate, so that their adhesion is weak. On the contrary, fcc(001) structures can have strong adhesion with the substrate if a large number of metal atoms is in contact with it. This is possible only if the nanodot shape is not compact. Finally, hcp structures better match the substrate, so that their adhesion is as strong with fewer atoms in contact. Shapes of hcp structures are thus more compact than those of fcc(001) structures, with a better E_{met}.

The tendency favoring hcp structures becomes more and more evident with increasing size. Our global optimization runs show that, in the size range $50 \leq N \leq 100$, hcp structures without stacking faults are the lowest in energy for 50 sizes over 51. The 5-fold motif becomes rapidly much higher in energy of both hcp and fcc(001) motifs and for sizes larger than 100 atoms can be safely ignored. At the same time, hcp structures with stacking faults become competitive, in agreement with the experimental observation.[16] In Figure 2 we show the global minimum structures for sizes $N =$ 100, 200, and 300. All these structures belong to the hcp motif and do not present stacking faults, even though there are faulted structures that are quite close in energy to the global minimum. For $N = 500$, four different structures are also shown: a hcp nanoparticle, a hcp nanoparticle with a stacking fault, a fcc structure, and an icosahedral structure. In the fcc structure, the facet in contact with the substrate is a vicinal of the (110) surface. The global minimum is the faulted hcp nanoparticle, which is separated by a small energy difference (0.12 eV) from the unfaulted hcp structure. The fcc and icosahedral structures are much higher than the global minimum, by 4.37 and 6.30 eV, respectively. The appearance of stacking faults in the hcp nanodots is not related to a better strain relief of the faulted structures with respect to the unfaulted ones. In fact, the faulted structures present a worse matching with the substrate, but a better metallic energy, because they produce fcc regions in the hcp nickel nanoparticle.

From the structures shown in Figure 2 the morphology of the hcp nanodots is quite easily understood. In

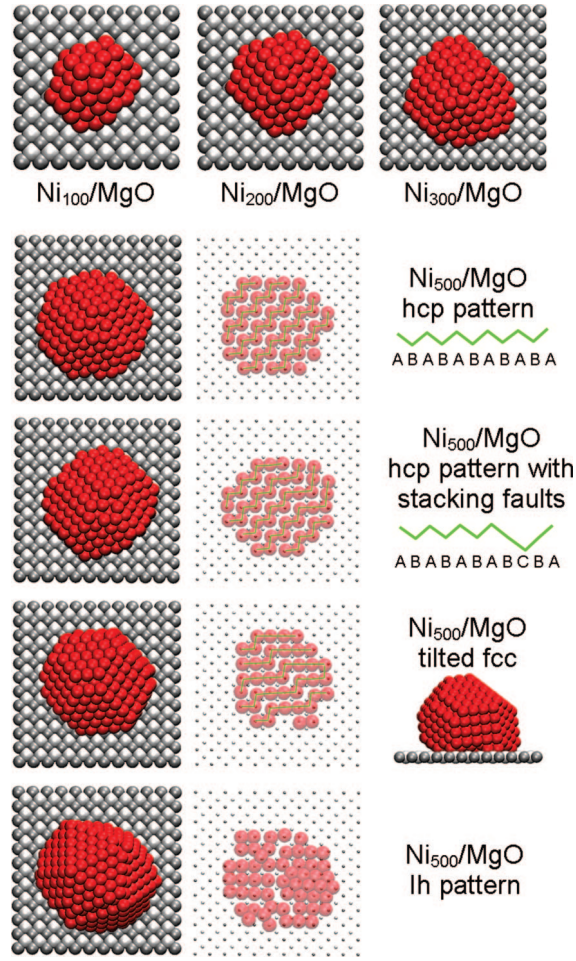

Figure 2. Global minima of Ni/MgO nanodots (of hcp structure) shown for $N = 100$, 200, and 300 atoms. For $N = 500$ we show, from top to bottom, an unfaulted hcp structure, a hcp structure with a stacking fault (global minimum), a fcc structure, and an icosahedral (Ih) structure.

fact, as better detailed in Figure 3, the hcp nanodots are truncated hexagonal bipyramids, whose axis coincides with the *c* axis of the hcp lattice. These bipyramids are cut to expose (0001), $(10\bar{1}1)$, and small $(11\bar{2}0)$ surfaces which offer a variety of adsorption sites of unusual geometry. In particular, the $(10\bar{1}1)$ facets present both 3-fold and 4-fold sites in close contact. A larger $(11\bar{2}0)$ face is in contact with the substrate, where Ni atoms assume a typical configuration in zigzag rows.

It is interesting to investigate the crossover from hcp to fcc(001) structures as size increases.[16,17] When size is above 500 atoms, full unseeded global optimization becomes more and more difficult, and practically not feasible for $N > 1000$.[22] Therefore we resort to the comparison of structures pertaining to the most competitive structural motifs: fcc(001) (in the form of truncated octahedra[17]) and hcp.

In order to compare the stability of the two motifs, we plot in Figure 4 the quantity $\Delta = (E_{bind} - N\epsilon_{Ni})/N^{2/3}$,[24] where E_{bind} is the total binding energy of the nanoparticle and ϵ_{Ni} is the binding energy per atom in bulk Ni. Δ is the excess energy of the nanoparticle with re-

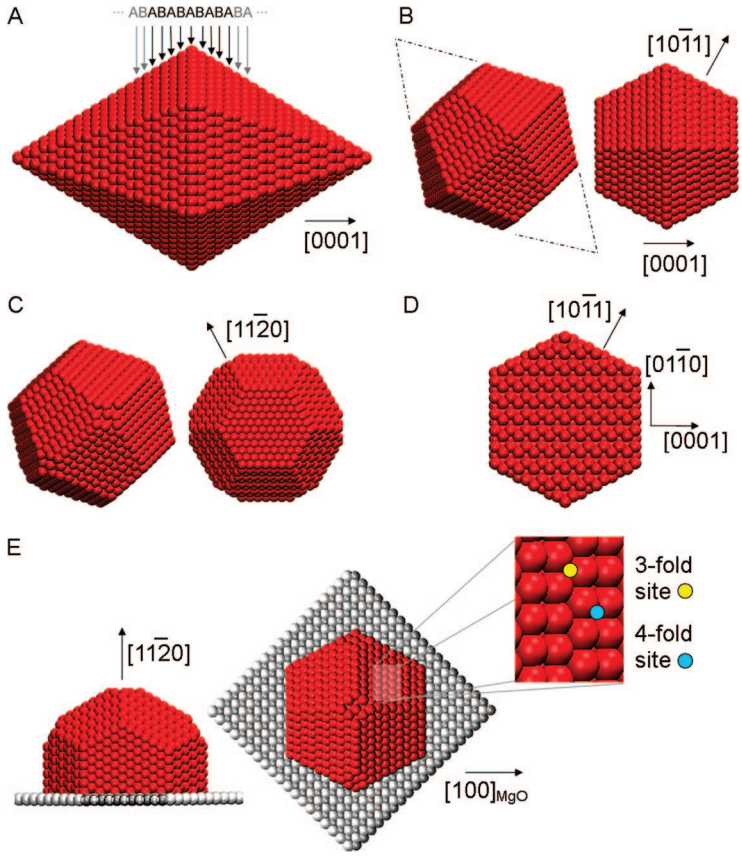

Figure 3. Morphology of the hcp motif. The hcp motif is obtained by truncating hexagonal bipyramids (A), whose axis is parallel to the *c*-axis of the hcp lattice of the metal. The first cut (B) eliminates top and bottom vertices of the pyramids, thus generating hexagonal (0001) faces. The second cut (C) eliminates lateral vertices, creating small (11$\bar{2}$0) facets, with their typical zigzag atomic arrangement. The final cut (D) is due to the contact with the substrate and generates a large (11$\bar{2}$0) face. Close-packed planes are perpendicular to the substrate. The nanodot is finally oriented in such a way that the [0001] direction of the hcp metal lattice is aligned with the [100] direction of the oxide substrate (E). The nanodot exposes also large (10$\bar{1}$1) facets, whose atomic arrangement is shown in the inset. These facets present a large number of 3-fold and 4-fold adsorption sites which are in close contact with each other.

which find the crossover for nanoparticles of thickness ~2.5 nm and lateral size ~5 nm.

What are the driving forces leading to the stabilization of the hcp nanodots? First of all, in these interface-stabilized phases, the hcp epitaxy is adopted to realize a good matching with the substrate. This geometric criterion is shown in Figure 5. Let d_1^{OO} and $d_2^{OO} = \sqrt{2}d_1^{OO}$ be the distances between first and second oxygen neighbors in the substrate, respectively. Let d^{MM} be the first neighbor distance in the bulk metal, $d^{apo} = \sqrt{3}d^{MM}$ the double of the apothema of 7-atom hexagons, and d^{AA} the distance between A planes in the hcp bulk. In an ideal hcp lattice, $d^{AA} = \sqrt{8/3}d^{MM}$. A good matching of the hcp phase is possible when both d^{apo}/d_2^{OO} and d^{AA}/d_2^{OO} are close to 1. For an ideal hcp lattice this implies that $d^{MM}/d^{OO} \simeq 0.8$. This condition warrants a bad matching of the fcc(001) epitaxy, for which $d^{MM}/d^{OO} \simeq 1$ should hold. Therefore, the fcc(001) epitaxy is automatically disfavored when the hcp (11$\bar{2}$0) epitaxy is favored. This makes it possible to stabilize hcp nanodots for fcc bulk metals, provided that the interaction with the substrate is sufficiently strong to overcome the energetic cost of building up the hcp phase. The second requirement to be fulfilled is that the hcp−fcc energy difference should not be too large. In this connection, we note that the above substrate-matching criterion is similar to that of the body-centered-cubic (bcc) (001) epitaxy. In fact, in the bcc(001) epitaxy, the metal atoms that are in contact with the substrate are at second neighbor distance $d_2^{MM} = 2d^{MM}/\sqrt{3}$. When $d^{apo}/d_2^{OO} \simeq 1$ and $d^{AA}/d_2^{OO} \simeq 1$, also $d_2^{MM}/d^{OO} \simeq 1$, so that a good hcp (11$\bar{2}$0) matching implies a good bcc(001) matching. However, bcc(001) epitaxy is strongly disfavored as a norm for metals which are not bcc in the bulk because of the much larger bcc−fcc energy difference with respect to the hcp−fcc one.[25] Finally, the (10$\bar{1}$1) faces should not be

spect to a bulk with the same number of atoms, approximately divided by the number of surface atoms. Lower values of Δ indicate more stable nanoparticles. The results in Figure 4 show that, for small sizes, the hcp motif presents lower Δ, as follows from the previously discussed global-optimization results. On the other hand, for large sizes, the fcc(001) motif must prevail[17] to recover the bulk fcc structure. A crossover between motifs is expected, and we find that it occurs between $N =$ 2000 and $N = 2500$ atoms, corresponding to nanodots 2.5 nm thick with lateral size of 4.5 nm, in very good agreement with the experimental results,[16]

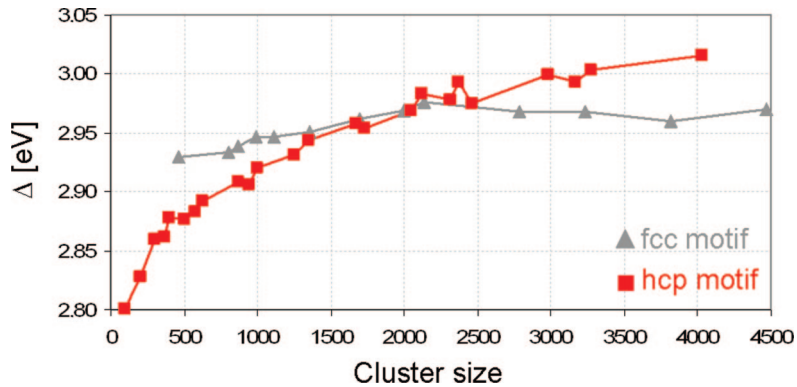

Figure 4. Crossover between structural motifs of nanodots. $\Delta = (E_{bind} - N\epsilon_{Ni})/N^{2/3}$ is plotted for the fcc(001) (A) and the hcp (B) motifs. A crossover from the hcp to the fcc(001) motif takes place for sizes between 2000 and 2500 atoms, corresponding to nanoparticle thickness of ~2.5 nm and width of ~4.5 nm.

too energetically disfavored with respect to (0001) faces, because the total area of the (10$\bar{1}$1) faces is large in the hcp nanodots.

Following these simple criteria, from the data reported in Table 2 we can predict the possible formation of hcp nanodots for several metal/substrate combinations, in particular Ni/MgO, Pd/CaO, Pt/CaO, Ni/CoO, and Co/MgO. The results of the DFT calculations nicely support these predictions: for each metal/oxide combination we have locally optimized several nanodot structures representative of the three main competitive structural families and found that the hcp motif is the lowest in energy for all systems at $N = 40$ and $N = 50$ for Co/MgO(001); see Table 3.

All these metals strongly adhere to their substrates. In Pd and Pt/CaO(001), the higher energy difference between hcp and fcc phases in Pd and Pt compared to Ni is partly compensated by the stronger adhesion to the CaO substrate and by the larger size mismatch of the fcc(001) epitaxy, which makes the latter quite unfavorable. The lattice parameter of CoO is very similar to that of MgO, so that the hcp Ni phase fits very well on the substrate, and the adhesion is even stronger than on MgO. As the nearest-neighbor distance in bulk Co is almost the same as in Ni, hcp Co/MgO(001) matches the substrate in the same way as Ni/MgO(001). The adhesion of Co to the substrate is comparable to that of Ni and moreover the hcp phase is marginally stable in Co bulk against the fcc phase (energy difference of about 0.004 eV/atom[25]).

In order to better discuss the factors determining the stability of hcp nanodots, we consider two more systems, for which we have not found evidence in favor of the hcp nanoparticle phase. The first counterexample is Pd/MgO. From Table 2 it follows that the fcc epitaxy better matches the substrate than the hcp epitaxy. In fact, as shown in ref 13, Pd/MgO nanodots are in fcc(001) epitaxy already starting from very small sizes, between 10 and 15 atoms. A second, and more interesting, counterexample is Au/CaO. Here, from the data in Table 2, the geometric criterion gives a very good matching of the hcp phase with the substrate. Moreover, the bulk hcp phase is only slightly higher in energy than the fcc phase. However, as reported in Table 3, the lowest energy Au_{40}/CaO cluster—a truncated rectangular pyramid—is in fcc(001) epitaxy with the substrate. This behavior of Au is due to the strong anisotropy of its surface energies, which favors clusters exposing close-packed surfaces. In Au, the ratio $\gamma_{(10\bar{1}1)}/\gamma_{(0001)}$ is large (see Table 2), disfavoring the hcp

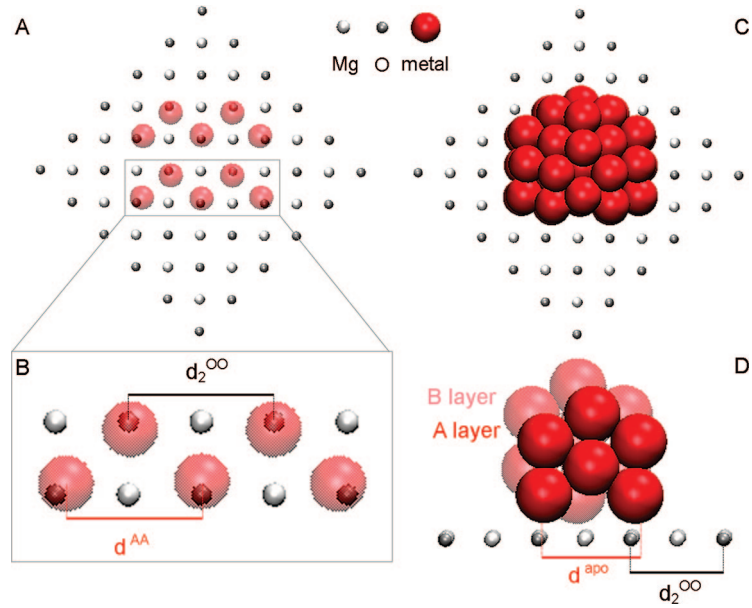

Figure 5. Matching of the hcp nanodots with the oxide surface. The criterion of good matching is that the distance between A planes in the hcp lattice (d^{AA}) and the apothema of 7-atom hexagons in the close-packed faces (d^{apo}) are both close to the distance between second-neighbor oxygens in the substrate (d_2^{OO}).

TABLE 2. Geometric Parameters for the Matching of the Nanodots with the Substrate[a]

metal	substrate	d^{apo}/d_2^{OO}	d^{AA}/d_2^{OO}	d^{MM}/d^{OO}	$\Delta E_{hcp-fcc}$	$\gamma_{(10\bar{1}1)}/\gamma_{(0001)}$
Ni	MgO(001)	1.024	0.964	0.837	1.1×10^{-2}	1.11
Co	MgO(001)	1.033	0.967	0.843	-4.4×10^{-3}	1.05
Pd	MgO(001)	1.135	1.068	0.927	2.1×10^{-2}	1.10
Pd	CaO(001)	0.992	0.935	0.810	2.1×10^{-2}	1.10
Pt	CaO(001)	1.001	0.943	0.817	2.6×10^{-2}	1.15
Au	CaO(001)	1.039	0.980	0.849	2.5×10^{-3}	1.22
Ni	CoO(001)	1.011	0.953	0.825	1.1×10^{-2}	1.11

[a]The data for calculating the geometric parameters are taken from ref 14. The experimental values of the energy difference (per atom) $\Delta E_{hcp-fcc}$ (in eV) between hcp and fcc bulk lattices are taken from ref 25. The ratios between surface energies $\gamma_{(10\bar{1}1)}/\gamma_{(0001)}$ are calculated by DFT.

TABLE 3. DFT Results on the Energetics of Co/MgO, Pd and Pt/CaO, and Ni/CoO Nanodots (All Energies in eV)

system and size	structure	E_{bind}	ΔE_{bind}	E_{adh}	E_{met}
Co_{30} /MgO(001)	fcc(001)	−111.22	0.00	−8.07	−103.15
	5-fold	−111.22	0.00	−7.56	−103.66
	hcp	−110.84	0.38	−7.14	−103.70
Co_{40} /MgO(001)	hcp	−151.18	0.00	−8.66	−142.52
	5-fold	−150.94	0.24	−8.41	−142.53
	fcc(001)	−149.62	1.56	−8.79	−140.83
Co_{50} /MgO(001)	hcp	−191.70	0.00	−10.72	−180.98
	5-fold	−191.39	0.31	−9.61	−181.78
	fcc(001)	−191.23	0.47	−10.15	−181.08
Pd_{40} /CaO(001)	hcp	−120.10	0.00	−10.55	−109.55
	fcc(001)	−119.30	0.80	−10.83	−108.47
	5-fold	−118.17	1.93	−8.58	−109.59
Pt_{40} /CaO(001)	hcp	−176.61	0.00	−14.46	−162.15
	fcc(001)	−174.64	1.97	−13.23	−161.41
	5-fold	−173.95	2.66	−12.89	−161.06
Au_{40} /CaO(001)	fcc(001)	−103.32	0.00	−7.20	−96.12
	hcp	−102.62	0.70	−6.87	−95.75
	5-fold	−102.50	0.82	−8.19	−94.31
Ni_{40} /CoO(001)	hcp	−158.90	0.00	−12.20	−146.70
	fcc(001)	−158.28	0.62	−12.57	−145.71
	5-fold	−158.09	0.81	−11.11	−146.98

nanodots with respect to fcc(001) pyramids, because the latter mostly expose close-packed faces.

Hcp metal-on-oxide nanodots are expected to present peculiar properties of interest in applications. As for the catalytic properties, recent research has clarified that catalysis is strongly affected not only by the type of nanoparticle facets (possibly in connection with the presence of particularly active sites[11]) but also by their relative orientation,[26] which can influence the mechanisms of mass transport over the nanoparticle surface. Shape is thus essential in determining the catalytic activity of metal nanoparticles, as shown, *e.g.*, by the enhanced catalytic activity of Pt nanocrystals with unconventional shapes, presenting facets of unusual geometries and orientations.[12] Moreover, the relative orientation of nanoparticle and substrate surfaces is known to play a role in both spillover and reverse spillover effects[27] and in adsorption modes of reacting molecules at the nanoparticle/oxide interface.[11] In this respect, the present hcp phases are very promising, as they exhibit unconventional features under all these viewpoints: the $(10\bar{1}1)$ facets have peculiar adsorption sites with unusual or strained coordination, they make unusual angles with the other, mostly close-packed, facets, and both the $(10\bar{1}1)$ and the close-packed facets present sharp interfaces with the oxide substrates, very different from the acute or obtuse angles of fcc pyramids or overhangs. The effect of all this on catalysis has still to be investigated.

As for magnetic properties, the easy magnetization axis in hcp structures is expected to be oriented along the *c* axis.[28] As a consequence of the 4-fold symmetry of the MgO(100) surface, the nanodot spin can thus be oriented along two different directions, making an angle of 90°. One can speculate that arrays of nanodots all oriented along the same direction could be obtained by applying a magnetic field during growth.[29] From the above discussion and Table 2, we also recall that a compression along the apothema and an elongation along the *c* axis are necessary to bring the nanodot structure in perfect registry with the oxide, and indeed these deformations are observed in the relaxed nanodot geometries, in perfect agreement with experiment. They should be beneficial in terms of magnetism, increasing the magnetic anisotropy of these systems.[28] Moreover, it is known that stacking faults decrease the magnetic anisotropy of hexagonal Co by provoking spin incoherence[30] and causing practical problems in applications, such as local bit storage instabilities and reading noise. The oxide substrate can stabilize against these phenomena, preventing the formation of fcc faults in the hcp lattice.

In conclusion, we have discussed a predictive computational methodology that allows one to study the size-dependent morphology of supported metal nanodots and applied it to metal particles on square-symmetry oxide surfaces in which the mismatch between the bulk metal nearest-neighbor distance and the O−O distance in the substrate is in the range 15−20%. We have shown that, in an appropriate range of adhesion and metallic energies, a general class of exotic hcp nanoparticle phases can be stabilized in a controlled way, even for metals that are not hcp in the bulk. These predictions have been supported by a comparison with available experimental data on Ni/MgO(100) nanodots, and generalized to a whole class of metal/oxide systems of great potential interest in catalytic and magnetic applications, such as Pd and Pt on CaO, and Ni and Co on CoO. To summarize, a morphological crossover has been quantitatively predicted, a general class of novel nanoparticle phases has been proposed, and the atomistic features of the particle structure have been unveiled for metal-on-oxide particles, features which in turn suggest that these materials might possess peculiar properties. This opens up a new avenue for predicting epitaxial relationships and tailoring structure and properties of supported metal nanoparticle nanophases *via* the substrate templating effect, a mechanism in principle extensible to other interfacial systems.

METHODS

As we deal with a very broad nanoparticle diameter range (1−8 nm), we use different computational methodologies depending on the size range considered. Three regimes can be spotted:

$N \leq 50$. Semiempirical model potentials are used within an unseeded global optimization approach to locate the most stable Ni/MgO(001) cluster structures. The significant structural motifs are singled out and, within each motif, several structures are locally relaxed by first-principle calculations.[22] Within this size range, DFT local minimizations extend the comparison among such motifs to the other metal/oxide systems considered in the paper;

$50 < N \leq 500$. The search for the lowest-energy structures is performed by an unseeded global optimization approach within semiempirical Ni/MgO(001) potential models;

$N > 500$. Candidate fcc and hcp clusters are built by truncating respectively fcc octahedra and hcp hexagonal bipyramids (see Figures 2 and 3). For each octahedron or bipyramid, several different truncations have been examined, in order to find the optimal one. Within semiempirical potential models, these nanoparticles are used as seeds for short global optimization searches, thus allowing full local structural relaxation and eventually small rearrangements of the structures, to accommodate the possible appeareance of dislocations.[17] The best structures that we have found have the same aspect ratios as those located by global optimization at smaller sizes, and are in reasonable agreement with the Wulff−Kaishew construction.[5]

In the following, the details of both energetic models and computational methods are discussed.

Energetic Modeling for Ni/MgO(001). In the global optimization searches, the energetic model is based on a tight-binding many-body potential for the metal−metal interactions and a surface energy potential approach fitted to *ab initio* calculations for the metal−oxide ones. The details of the energetic model description can be found in refs 17 and 23 together with the form of the metal−oxide interaction. The parameters for the Ni−MgO(001) interaction are listed in ref 31.

Concerning metal−metal interactions, their functional form is derived within the second-moment approximation to the

tight-binding model (SMATB potential). Within this approach, the total energy E_c of the system is obtained as[32]

$$E_c = \sum_i (E_b^i + E_r^i) \quad (1)$$

with

$$E_r^i = \sum_{j \neq i, r_{ij} < r_c} A \exp\left[-p\left(\frac{r_{ij}}{r_0} - 1\right)\right] \quad (2)$$

$$E_b^i = -\left\{\sum_{j \neq i, r_{ij} < r_c} \xi^2 \exp\left[-2q\left(\frac{r_{ij}}{r_0} - 1\right)\right]\right\}^{1/2} \quad (3)$$

where r_{ij} is the distance between atoms i and j, r_c is the cutoff radius, r_0 is the nearest-neighbor distance. The parameter set (A, ξ, p, q) fitted to experimental bulk quantities. We fit the equilibrium nearest-neighbor distance in bulk Ni, the bulk binding energy per atom E_{bind}, the bulk modulus B, and the experimental value of the energy difference (per atom) $\Delta E_{hcp-fcc}$ between hcp and fcc bulk lattices. The potential is smoothly linked to zero between the 5th and 6th neighbor distances by a polynomial function. The values of the parameters are A = 0.084 470 25 eV, ξ = 1.404 973 55 eV, p = 11.73, q = 1.93. The validity of our SMATB parametrization has been checked against experimental and DFT results for what concerns surface energies of high-index surfaces and equilibrium distances in small clusters, obtaining a good agreement.

Also other parametrizations of the SMATB potential[33,34] have been used in order to build up a richer database of oxide-supported structures by means of global optimization searches. For Pd and Pt/CaO(001) nanoparticles also motifs from our Pd and Pt/MgO(001) databases[13] were considered.

Density Functional Theory (DFT) Calculations. The DFT calculations are carried out using the PWscf (plane-wave self-consistent field) computational code,[35] employing the PBE xc-functional[36] and ultrasoft pseudopotentials in the spin-unrestricted formalism. The MgO(001) surface is modeled by a two-layer slab, each layer containing 25 Mg(Ca) and 25 O atoms, 5 × 5 cell, fixed in the lattice positions of the rock salt bulk structure of the various oxides. The distance between replicated cells in the direction perpendicular to the (001) surface is about 13 Å, and implies a distance of at least ≈6 Å between atoms in replicated cells. The kinetic energy cutoff for the selection of the plane-wave basis set is fixed at 30 Ryd (1 Ryd = 13.6 eV) for the energy and 150 Ryd for the density in all the calculations. Because of the large dimensions of the unit cell, eigenvalues and eigenvectors of the Kohn−Sham Hamiltonian are only evaluated at the Γ point. A Gaussian smearing technique[37] (with a smearing parameter of 0.002 Ryd) is applied. Bulk CoO has an antiferromagnetic spin ground state. As in analogous transition metal oxide systems, gradient-corrected xc-functionals, including the PBE one,[36] erroneously predict the ground state of CoO to be metallic,[38] a behavior usually cured *via* the use of DF+U[39] or hybrid-exchange[40] techniques within the DF formalism. To reduce the computational effort within the limit of our possibilities, we nevertheless chose to use the PBE xc-functional also in the CoO case: the antiferromagnetic state is anyway the ground state at the DF level, and a proper magnetic state for the oxide layer (even after the adsorption of ferromagnetic Ni clusters) can be simply obtained by doubling the unit cell (space group $R\bar{3}m$ in the bulk) and providing the right starting magnetization on each Co atom. This, however, implied that a 6 × 6 cell had to be used in this case. This choice is supported by selected calculations showing that the metal−surface interaction depends only marginally on the spin state of the oxide, and by the fact that the total density of the system is essentially correctly predicted by GGA approaches.[41]

Global Optimization Methods. The global optimization searches are performed by means of the basin hopping (BH) algorithm[42] and the parallel excitable walkers (PEW) algorithm.[43] For any nanoparticle size N below 100 atoms, 3−5 unseeded searches of 50 000 steps each are performed. Unseeded searches are started from random positions in a cubic box placed above the oxide surface. In the range $100 < N < 200$, we have considered only sizes 100, 110, 120,..., 200. For each size, at least 10 unbiased searches have been performed. We have run 15 unbiased searches for sizes N = 300 and 500. Moreover, several shorter seeded searches are performed. Seeded searches may either start from structures pertaining to motifs found at nearby sizes (typically $N - 1$ and $N + 1$ atoms), or from structures found at the same size within searches by means of a different potential parametrization (see ref 22 for a review on the global optimization methods). In the PEW searches, we use as an order parameter the fraction of atoms that are in contact with the substrate.

Acknowledgment. We thank Claude Henry for a critical reading of the manuscript. We acknowledge financial support from the European Community Sixth Framework Programme for the GSOMEN project (NMP4-CT-2004-001594). G.R. acknowledges *L'Oréal Italia e UNESCO per le Donne e la Scienza*, 2007 edition, for a research fellowship.

REFERENCES AND NOTES

1. Burda, C.; Chen, X.; Narayanan, R.; El-Sayed, M. A. Chemistry and Properties of Nanocrystals of Different Shapes. *Chem. Rev.* **2005**, *105*, 1025–1102.
2. Lord, E. A.; Mackay, A. L.; Ranganathan, S. *New Geometries for New Materials*; Cambridge University Press: Cambridge, UK, 2006.
3. Li, J.; Li, X.; Zhai, H.-J.; Wang, L. S. Au_{20}: a Tetrahedral Cluster. *Science* **2003**, *299*, 864–867.
4. Rossi, G.; Rapallo, A.; Mottet, C.; Fortunelli, A.; Baletto, F.; Ferrando, R. Magic Polyicosahedral Core-Shell Nanoclusters. *Phys. Rev. Lett.* **2004**, *93*, 105503-1–105503-4.
5. Henry, C. R. Morphology of Supported Nanoparticles. *Prog. Surf. Sci.* **2005**, *80*, 92–116.
6. Renaud, G.; Lazzari, R.; Revenant, C.; Barbier, A.; Noblet, M.; Ulrich, O.; Leroy, F.; Jupille, J.; Borensztein, Y.; Henry, C. R.; et al. Real-Time Monitoring of Growing Nanopar- ticles. *Science* **2003**, *300*, 1416–1419.
7. Libuda, J.; Freund, H.-J. Molecular Beam Experiments on Model Catalysts. *Surf. Sci. Rep.* **2005**, *57*, 157–298.
8. Valden, M.; Lai, X.; Goodman, D. W. Onset of Catalytic Activity of Gold Clusters on Titania with the Appearance of Nonmetallic Properties. *Science* **1998**, *281*, 1647–1650.
9. Campbell, C. T.; Parker, S. C.; Starr, D. E. The Effect of Size-Dependent Nanoparticle Energetics on Catalyst Sintering. *Science* **2002**, *298*, 811–814.
10. Judai, K.; Abbet, S.; Worz, A. S.; Heiz, U.; Henry, C. R. Low-Temperature Cluster Catal- ysis. *J. Am. Chem. Soc.* **2004**, *126*, 2732–2737.
11. Molina, L. M.; Hammer, B. Some Recent Theoretical Advances in the Understanding of the Catalytic Activity of Au. *Appl. Catal., A* **2005**, *291*, 21–31.
12. Xiong, Y.; Wiley, B. J.; Xia, Y. Nanocrystals with Unconventional Shapes—a Class of Promising Catalysts. *Angew. Chem. Intl. Ed.* **2007**, *46*, 7157–7159.
13. Barcaro, G.; Fortunelli, A.; Rossi, G.; Nita, F.; Ferrando, R. Epitaxy, Truncations and Overhangs in Palladium Nanoclusters Adsorbed on MgO(001). *Phys. Rev. Lett.* **2007**, *98*, 156101-1–156101-4.
14. *Landolt-Börnstein Tables*; Hellwege, K.-H., Hellwege, A. M., Eds.; Springer: Berlin, 1975; Group III, Vol. 7b.
15. Pacchioni, G.; Rosch, N. Supported Nickel and Copper Clusters on MgO(100): a First- Principles Calculation on the Metal/Oxide Interface. *J. Chem. Phys.* **1996**, *104*, 7329–7337.
16. Tian, W.; Sun, H. P.; Pan, X. Q.; Yu, J. H.; Yeadon, M.; Boothroyd, C. B.; Feng, Y. P; Lukaszew, R. A.; Clarke, R. Hexagonal Close-Packed Ni Nanostructures Grown on the (001) Surface of MgO. *Appl. Phys. Lett.* **2005**, *86*, 131915-1–131915-3.
17. Sao-Joao, S.; Giorgio, S.; Mottet, C.; Goniakowski, J.; Henry, C. R. Interface Structure of Ni Nanoparticles on MgO(100): a Combined HRTEM and Molecular Dynamics Study. *Surf. Sci.* **2006**, *600*, L86–L90.

18. Allegretti, F.; Parteder, G.; Ramsey, M. G.; Surnev, S.; Netzer, F. P. The Formation of Sharp NiO(100)-Cobalt Interfaces. *Surf. Sci.* **2007**, *601*, L73–L76.
19. Nogués, J.; Schuller, I. K. Exchange Bias. *J. Magn. Magn. Mat.* **1999**, *192*, 203–232.
20. Kitakami, O.; Sato, H.; Shimada, Y.; Sato, F.; Tanaka, M. Size Effect on the Crystal Phase of Cobalt Fine Particles. *Phys. Rev. B* **1999**, *56*, 13849–13854.
21. Morel, R.; Brenac, A.; Bayle-Guillemaud, P.; Portemont, C.; La Rizza, F. Growth and Properties of Cobalt Clusters Made by Sputtering Gas-Aggregation. *Eur. Phys J. D* **2003**, *24*, 287–290.
22. Ferrando, R.; Fortunelli, A.; Johnston, R. L. Searching for the Optimum Structures of Alloy Nanoclusters. *Phys. Chem. Chem. Phys.* **2008**, *10*, 640–649.
23. Vervisch, W.; Mottet, C.; Goniakowski, J. Theoretical Study of the Atomic Structure of Pd Nanoclusters Deposited on a MgO(100) Surface. *Phys. Rev. B* **2002**, *65*, 245411-1–245411-9.
24. Cleveland, C. L.; Landman, U.; Schaaff, T. G.; Shafigullin, M. N.; Stephens, P. W.; Whetten, R. L. Structural Evolution of Smaller Gold Nanocrystals: the Truncated Decahedral Motif. *Phys. Rev. Lett.* **1997**, *79*, 1873–1876.
25. Dinsdale, A. T. SGTE Data for Pure Elements. *CALPHAD* **1991**, *15*, 317–425.
26. Oŝterlund, L.; Grant, A. W.; Kasemo, B. Lithographic Techniques in Nanocatalysis. In *Nanocatalysis, Series: NanoScience and Technology*; Heiz, U., Landman, U., Eds.; Springer Verlag: Berlin, 2007.
27. Rottgen, M. A.; Abbet, S.; Judai, K.; Antonietti, J. M.; Worz, A. S.; Arenz, M.; Henry, C. R.; Heiz, U. Cluster Chemistry: Size-Dependent Reactivity Induced by Reverse Spill-Over. *J. Am. Chem. Soc.* **2006**, *129*, 9635–9639.
28. Hashimoto, A.; Saito, S.; Itagaki, N.; Takahashi, M. Pseudo-hcp Nonmagnetic Intermediate Layer for Granular Media with High Perpendicular Magnetic Anisotropy. *J. Phys. D: Appl. Phys.* **2008**, *41*, 012002−1012002−4.
29. Einax, M.; Heinrichs, S.; Maass, P.; Majhofer, A.; Dieterich, W. Simulation of MBE- Growth of Alloy Nanoclusters in a Magnetic Field. *Mater. Sci. Eng., C* **2007**, *27*, 1325–1327.
30. Sort, J; Suriñach, S.; Muñoz, J. S.; Bar, M. D.; Wojcik, M.; Jedryka, E.; Nadolski, S.; Sheludko, N.; Nogués, J. Role of Stacking Faults in the Structural and Magnetic Properties of Ball-Milled Cobalt. *Phys. Rev. B* **2003**, *68*, 014421-1–014421-7.
31. Mottet, C.; Goniakowski, J. http://www.cinam.univ-mrs.fr/mottet/param/metalMgO.pdf.
32. Gupta, R. P. Lattice Relaxation at a Metal Surface. *Phys. Rev. B* **1985**, *23*, 6265–6270.
33. Cleri, F.; Rosato, V. Tight-Binding Potentials for Transition Metals and Alloys. *Phys. Rev. B* **1993**, *48*, 22–33.
34. López, M-J.; Jellinek, J. On the Problem of Fitting Many-Body Potentials. I. The Minimal Maximum Error Scheme and the Paradigm of Metal Systems. *J. Chem. Phys.* **1999**, *110*, 8899–8911.
35. Baroni, S.; Dal Corso, A.; de Gironcoli, S.; Giannozzi, P. http://www.pwscf.org.
36. Perdew, J. P.; Burke, K.; Ernzerhof, M. Generalized Gradient Approximation Made Simple. *Phys. Rev. Lett.* **1996**, *77*, 3865–3868.
37. Elsässer, C.; Fähnle, M.; Chan, C. T.; Ho, K. M. Density-Functional Energies and Forces with Gaussian-Broadened Fractional Occupations. *Phys. Rev. B* **1994**, *49*, 13975–13978.
38. Dufek, P.; Blaha, P.; Sliwko, V.; Schwarz, K. Generalized-Gradient-Approximation Description of Band Splittings in Transition-Metal Oxides and Fluorides. *Phys. Rev. B* **1994**, *49*, 10170–10175.
39. Anisimov, V. I.; Zaanen, J.; Andersen, O. K. Band Theory and Mott Insulators: Hubbard U Instead of Stoner I. *Phys. Rev. B* **1991**, *44*, 943–954.
40. Feng, X. Electronic Structure of MnO and CoO From the B3LYP Hybrid Density Functional Method. *Phys. Rev. B* **2004**, *69*, 155107-1–155107-7.
41. Fritsche, L.; Koller, J.; Reinert, T. Borderline Cases in Density Functional Theory. *Int. J. Quantum Chem.* **2004**, *100*, 681–694.
42. Wales, D. J.; Doye, J. P. K. Global Optimization by Basin-Hopping and the Lowest Energy Structures of Lennard-Jones Clusters Containing up to 110 Atoms. *J. Phys. Chem. A* **1997**, *101*, 5111–5116.
43. Rossi, G.; Ferrando, R. Global Optimization by Excitable Walkers. *Chem. Phys. Lett.* **2006**, *423*, 17–22.